Magnetized ablative Rayleigh-Taylor instability in three dimensions

C. A. Walsh ◉ [*]

Lawrence Livermore National Laboratory, Livermore, California 94550, USA

Three-dimensional extended-magnetohydrodynamics simulations of the magnetized ablative Rayleigh-Taylor instability are presented. Previous two-dimensional (2D) simulations claiming perturbation suppression by magnetic tension are shown to be misleading, as they do not include the most unstable dimension. For perturbation modes along the applied field direction, the magnetic field simultaneously reduces ablative stabilization and adds magnetic tension stabilization; the stabilizing term is found to dominate for applied fields > 5 T, with both effects increasing in importance at short wavelengths. For modes perpendicular to the applied field, magnetic tension does not directly stabilize the perturbation but can result in moderately slower growth due to the perturbation appearing to be 2D (albeit in a different orientation to 2D inertial confinement fusion simulations). In cases where thermal ablative stabilization is dominant the applied field increases the peak bubble-spike height. Resistive diffusion is shown to be important for short wavelengths and long timescales, reducing the effectiveness of tension stabilization.

I. INTRODUCTION

Magnetic fields can be applied to inertial confinement fusion (ICF) implosions to reduce hot-spot energy losses by magnetizing the electron population. This was demonstrated for direct-drive implosions at the OMEGA Laser Facility, where an 8 T applied field increased the yield and temperature of a spherical capsule by 30% and 15%, respectively [1]. An externally applied field has also been predicted to bring current best-performing implosions on the National Ignition Facility (NIF) into the burning plasma regime [2,3]. Magnetized Liner Inertial Fusion (MagLIF) experiments on the Z Pulsed Power Facility are designed specifically with the use of an external magnetic field, allowing for slower and higher-adiabat designs [4]; two-dimensional (2D) simulations predict yield amplifications by magnetization of > 100 when sufficient laser preheat energy is used [5]. In parallel, a campaign using a scaled-down version of MagLIF is underway on OMEGA [6]. It is also thought that an applied magnetic field can assist fast ignition designs, as the field allows for enhanced coupling of charged particle beams to the hot spot [7]

While the main focus of research to date has been on the effect of magnetic fields on the bulk hot-spot performance, it is important to also consider how magnetizing the plasma can change deceleration-phase perturbation growth. Two-dimensional simulations have predicted the reduction of Rayleigh-Taylor instability due to magnetic tension [2,8,9]. As magnetic tension preferentially stabilizes short wavelength perturbations [10], it has been suggested that mixing could be reduced by the application of a magnetic field [9]. Other simulations have demonstrated that an applied field reduces the ablation of perturbations and can therefore also decrease stability [11].

This paper presents three-dimensional (3D) magnetized-ablative-Rayleigh-Taylor (MARTI) instability simulations, demonstrating that a 2D approach always ignores the least stable dimension. Magnetic tension cannot completely stabilize the Rayleigh-Taylor instability, as the field suppresses modes only where $\underline{k} \cdot \underline{B} \neq 0$. Instead, a large magnetic field is found to, at best, only moderately reduce perturbation growth ($\approx 1/3$ when thermal conduction is less important) and, at worst, significantly enhance short wavelength perturbation growth. This result, among others, has significant implications for the design of magnetized ICF implosions, where 2D simulations are routinely employed (e.g., OMEGA spherical [12], OMEGA cylindrical [13,14], NIF spherical [2,3], MagLIF cylindrical [5,15–17], and fast ignition spherical [18] implosions).

The 3D nature of the Rayleigh-Taylor instability with an embedded magnetic field was studied previously in astrophysical plasmas [19]; similar to the current work, the magnetic field was found to stabilize the instability only along field lines, resulting in a striated unstable interface. The distinction of the work presented here is the applicability to ICF implosions, for which ablation of dense material is key to tamping the instability growth.

The classical Rayleigh-Taylor instability, in which a low density fluid is accelerated into a higher density fluid, is maximally unstable at short perturbation wavelengths [20,21]. The growth rate in the short wavelength limit ($\lambda \ll L_\rho$, where λ is the perturbation wavelength and $L_\rho = \rho/\nabla\rho$ is the density scale length) can be found by simple energy conservation. Balancing the kinetic energy of the instability growth [$\rho(\partial h/\partial t)^2/2$, where h is the spike-bubble height] with the gravitational potential energy gained by the spike ($\nabla\rho gh^2/2$, where g is the acceleration) gives an exponential perturbation

[*]Corresponding author: walsh34@llnl.gov

growth rate:

$$\gamma_{\text{RTI}} = \sqrt{\frac{g}{L_\rho}}. \tag{1}$$

However, energy transport from the light to the dense fluid can induce mass ablation, which stabilizes the Rayleigh-Taylor growth [22], particularly for short perturbation wavelengths. This is then called the ablative Rayleigh-Taylor instability (ARTI), where the highest modes are classically unstable but also the most stabilized by ablation. In an ICF hot spot this ablation manifests primarily through electron thermal conduction from the hot-spot core to the dense assembled fuel, although radiation transport and α heating also contribute [23]. When the ablation is dominated by thermal conduction, V_{abl} is proportional to the thermal conductivity κ. This can be shown simply by quantifying the volume of cold plasma heated up to the core hot-spot temperature every second ($\Delta T n_e V_{\text{abl}} \delta S$) by heat flow ($\delta S \kappa \nabla T_e$) through a surface ($\delta S$). This yields [24]

$$V_{\text{abl}} \sim \frac{\kappa^c T^{5/2}}{L_T \rho}, \tag{2}$$

where κ^c is the nondimensional thermal conductivity that is independent of temperature T and density ρ. L_T is the temperature length scale (proportional to the hot-spot radius for ICF implosions). If the ablation occurred uniformly across the unstable interface, it would not change the bubble or spike height. However, the spikes are more exposed to hot plasma than the bubbles, resulting in more ablation of spikes (and less ablation of bubbles), thereby lowering overall growth. The normalized difference in the nearby hot plasma volume between spikes and bubble scales with h/λ. Using $(\partial h/\partial t)_{\text{ARTI}} = (\partial h/\partial t)_{\text{RTI}} - h V_{\text{abl}}/\lambda$ and Eq. (2) gives a reduced growth rate for the ARTI:

$$\gamma_{\text{ARTI}} = \sqrt{\frac{g}{L_\rho} - \frac{a \kappa^c T^{5/2}}{L_T \rho \lambda}}, \tag{3}$$

where a is a constant that depends on the geometry and plasma composition [24]. This shows that the ablative stabilization is strongest for high temperature plasmas and perturbations with short wavelengths [25].

Magnetized heat flow in an magnetohydrodynamics (MHD) plasma follows [26,27]

$$\underline{q} = -\kappa_\parallel (\hat{\underline{b}} \cdot \nabla T_e) \hat{\underline{b}} - \kappa_\perp \hat{\underline{b}} \times (\nabla T_e \times \hat{\underline{b}}) - \kappa_\wedge \hat{\underline{b}} \times \nabla T_e, \tag{4}$$

where $\hat{\underline{b}}$ is the magnetic field unit vector. The first term ($\kappa_\parallel$) represents unrestricted heat flow along magnetic field lines. The second term ($\kappa_\perp$) is the heat flow perpendicular to the field and is suppressed by magnetization. The Hall parameter $\omega_e \tau_e$ is a metric for the degree of magnetization, a product of the electron gyrofrequency ω_e and electron-ion collision time τ_e. If a magnetic field is applied along the ARTI spike propagation axis, then the thermal conductivity in Eq. (3) is $\kappa_\parallel^c$ and is unaltered by the electron magnetization. If the magnetic field is applied perpendicular to the spike propagation axis, then the thermal conductivity in Eq. (3) is $\kappa_\perp^c$, and the ablation velocity is suppressed by electron magnetization, decreasing the ablative stabilization. This can be summarized by using $\kappa^c = |\hat{\underline{b}} \cdot \hat{\underline{n}}| \kappa_\parallel^c + (1 - |\hat{\underline{b}} \cdot \hat{\underline{n}}|) \kappa_\perp^c$ in Eq. (3), where $\hat{\underline{b}}$ is

the magnetic field unit vector and $\hat{\underline{n}}$ is the unstable interface unit normal.

The final term ($\kappa_\wedge$) in Eq. (4) is Righi-Leduc heat flow, which acts perpendicular to both the magnetic field and the temperature gradient. This term is largest for moderate magnetizations $\omega_e \tau_e \approx 1$. The effect of this component is less clear than the parallel or perpendicular components and does not affect the overall ablation velocity. Instead, the Righi-Leduc term is found to break the ablation velocity symmetry, resulting in spikes not propagating directly along the acceleration axis.

A magnetic field embedded in the plasma can also introduce a dynamically important Lorentz force ($\underline{j} \times \underline{B}$, where $\underline{j}$ is the current density). Typically, the importance of the Lorentz force is characterized by the plasma β, which is the ratio of the thermal plasma pressure to the magnetic pressure. However, this can be misleading, as it assumes that the thermal pressure and the magnetic potential vary over the same scale length [11]. The Lorentz force can be split into two components: a magnetic pressure [$\nabla(\underline{B} \cdot \underline{B})/2\mu_0$] and a magnetic tension ($\underline{B} \cdot \nabla \underline{B}/\mu_0$). This latter term acts to straighten the magnetic field lines and is strongest over short wavelengths [9,10]. While high magnetic pressures in the hot spot can reduce compression [14,28], the magnetic tension is typically greatest around perturbations and can reduce vorticity [11].

The stabilizing effect of the magnetic tension on the instability can be shown through simple energetic arguments. The change in magnetic field along a field line over half a wavelength is equal to $2|B|h/\lambda$ (for $h < \lambda$), giving a tension force $4|B|^2 h/\lambda^2$. The work done by the spike or bubble in moving a distance $h/2$ is then included in the energy balance to give a linear MARTI growth rate:

$$\gamma_{\text{MARTI}} = \sqrt{\frac{g}{L_\rho} - \frac{4|\underline{B}|^2 |\hat{\underline{b}} \cdot \hat{\underline{k}}|}{\mu_0 \rho \lambda^2} - \frac{a \kappa^c T^{5/2}}{L_T \rho \lambda}}, \tag{5}$$

where $\hat{\underline{b}}$ is the magnetic field unit vector and $\hat{\underline{k}}$ is the unit mode vector ($|\hat{\underline{k}}| = 1$) with the direction along the perturbation interface. The factor $|\hat{\underline{b}} \cdot \hat{\underline{k}}|$ represents the fact that magnetic tension stabilizes only perturbation growth that bends the field lines. Suppression of instabilities along magnetic field lines has been demonstrated experimentally using gas-puff Z pinches [8,29,30].

The work presented here focuses on nonlinear perturbations propagating perpendicular to the magnetic field orientation, which is applicable to the capsule waist of spherical implosions and everywhere for cylindrical designs with an axial magnetic field. The axis of spike growth is designated $\underline{z}$, while the magnetic field is oriented in $\underline{x}$. In this orientation magnetic tension acts against spike growth and also suppresses thermal conduction into the spike. While the thermal conduction is anisotropic (i.e., there is unrestricted heat flow in $\underline{x}$ but not in y), this particular effect is not found to induce anisotropic perturbation growth. The magnetic tension, on the other hand, is found to suppress perturbations with short wavelengths in $\underline{x}$ but not in y.

Another orientation relevant to the poles of magnetized spherical implosions is a magnetic field parallel to spike growth; previous simulations have shown that an increased hot-spot temperature can result in enhanced heat flow at the

spherical poles, resulting in lower perturbation growth [11]. However, in this configuration the field tension does not significantly modify the Rayleigh-Taylor instability, as the spike does not perturb the background field. For this reason, the work in this paper focuses on the case where the magnetic field is applied perpendicular to spike growth.

The work here also focuses on perturbation growth during the stagnation phase; applied fields are also expected to modify direct-drive perturbation growth during the drive phase through magnetization of the laser conduction zone [31]. In indirect drive, where radiation transport dominates over thermal conduction, an applied magnetic field does not modify the ablation process.

The 3D extended-MHD code GORGON [32–34] is used for this study. The simulations include magnetic transport by bulk advection, Nernst, cross-gradient-Nernst, and resistive diffusion [35]. Magnetic fields generated by the Biermann battery mechanism and from ionization gradients [36] are included; GORGON has been used extensively to study self-generated magnetic fields in the deceleration phase of ICF implosions [34,37,38]. The Biermann battery term in GORGON has been benchmarked against magnetic fields observed in laser-foil interaction experiments [39,40]. Improvements to the Epperlein and Haines [41] transport coefficients [27], which have been shown to reduce the effect of magnetic field twisting in scenarios relevant to this paper [38], are used. The magnetic transport in GORGON has been successfully compared with cylindrical implosions probed by high energy protons [42], with particular sensitivity to bulk plasma advection and the Nernst term [14]. Thermal transport is treated anisotropically using a centered-symmetric scheme [43], which has been modified to include Righi-Leduc heat flow; this scheme reduces erroneous diffusion of heat across the magnetic field lines [43,44]. The Lorentz force is included, as well as Ohmic dissipation of magnetic energy. No radiation transport is included in these calculations, which greatly increases the number of possible simulations in three dimensions. Spatial resolution of $1/2\,\mu$m is used in $\underline{x}$ and $\underline{y}$ in order to resolve the shortest wavelengths, while $1\,\mu$m resolution in $\underline{z}$ was found to be adequate for converged Rayleigh-Taylor growth.

The 3D MARTI test problem uses the constant acceleration $g = 10^{15}\,\text{m/s}^2$ of a planar low density deuterium plasma (initial density $\rho_0 = 10^3\,\text{kg/m}^3$) into a dense deuterium plasma ($\rho_0 = 10^4\,\text{kg/m}^3$). At $t = 0$ a $d = 200\,\mu$m transition layer between the two densities is used such that the density follows an exponential decay. The temperature of the low density plasma is initialized at $T_0 = 200\,\text{eV}$, with the high density plasma temperature set isobarically. Periodic boundary conditions are employed in these Cartesian simulations. The density gradient is set along $+\underline{z}$, while the acceleration is directed along $-\underline{z}$.

The setup inputs (g, ρ_0, $\Delta\rho_0$, T_0, d) were tuned to recreate the key parameters of a decelerating hot spot. By $t = 1.6$ ns the peak density and temperatures are $10^5\,\text{kg/m}^3$ and 4100 eV, with $\approx 100\,\mu$m distance between the two peaks. At $t = 1.9$ ns the peak density and temperature increase to $1.4 \times 10^5\,\text{kg/m}^3$ and 5700 eV. Perturbation growth results are presented at both 1.6 and 1.9 ns, with thermal ablative stabilization being more important for the later time.

A perturbation is applied by offsetting the transition layer between the dense and light plasma regions. For the single-mode perturbations this is an amplitude of 5 μm, while the multimode calculations use 500 randomly placed perturbations with random wavelengths and random amplitudes with a maximum of ϵ each, where ϵ is varied between 0.2 and 1.0 μm to assess the dependence of the observed phenomena on perturbation size.

The magnetic field is applied along $\underline{x}$ using a strength proportional to the plasma density. This is in accordance with how the magnetic field would be compressed in planar or cylindrical geometry if the field is frozen into the plasma. The quoted applied magnetic field B_0 is the field strength that began in unheated ice $|\underline{B}| = B_0\rho/\rho_{\text{ice}}$, where $\rho_{\text{ice}} = 250\,\text{kg/m}^3$. For example, $B_0 = 5$ T actually corresponds to an initialized field of 20 T in the low density plasma and 200 T in the high density plasma. For a spherical implosion the initial field will scale more weakly with density [$|\underline{B}| = B_0(\rho/\rho_{\text{ice}})^{2/3}$], although the results are found to be qualitatively similar.

Section II first demonstrates the 3D nature of the magnetized-ablative-Rayleigh-Taylor instability. The height of the spike along the magnetic field h_x is shown to be much lower than the height perpendicular to the magnetic field h_y when the magnetic tension is significant. Both temporal and wavelength dependences are explored in detail, showing the greatest perturbation anisotropy h_y/h_x for short wavelength perturbations. Resistive diffusion is also shown to play an important role in spike height along the field lines h_x. Section III then demonstrates striated growth with multimode perturbations applied. An applied magnetic field is shown to reduce peak spike-bubble heights (i.e., both h_x and h_y) for smaller initialized perturbations, analogous to moderate reductions in RTI growth rates in 2D systems relative to 3D systems.

II. SINGLE-MODE PERTURBATIONS

Single-mode perturbations are applied using a 5 μm amplitude cosine function, resulting in a spike down the simulation axis. Figure 1 shows $\rho = 6 \times 10^4\,\text{kg/m}^3$ density contours for $B_0 = 0$ T and $B_0 = 50$ T at 1.6 ns for a perturbation wavelength of 25 μm. In the magnetized case some magnetic field streamlines have been plotted to demonstrate the magnetic field bending. For 50 T the spike is almost completely suppressed when looking along the $\underline{x}$ direction, which is consistent with previous 2D claims of Rayleigh-Taylor suppression [2,9]. The magnetic field at this time is over 10^4 T in strength, with an estimated minimum unstable perturbation wavelength [from Eq. (5)] of 15 μm, which is similar to the actual wavelength of 20 μm. Note that the plasma β at this time is over 10 everywhere, which suggests that the Lorentz force is only of secondary importance; this highlights that the plasma β is misleading when dealing with magnetic tension effects.

While the perturbation is almost completely suppressed along the magnetic field direction, the total bubble-spike height remains similar to the unmagnetized case. In the $\underline{y}$ direction the spike is able to push between magnetic field lines. In other words, large amplitudes in $\underline{y}$ do not result in the bending of magnetic field lines, and there is no tension force to suppress growth.

Figure 2 shows the temporal dependence of the spike-bubble height in $\underline{x}$ and $\underline{y}$ for a perturbation of wavelength
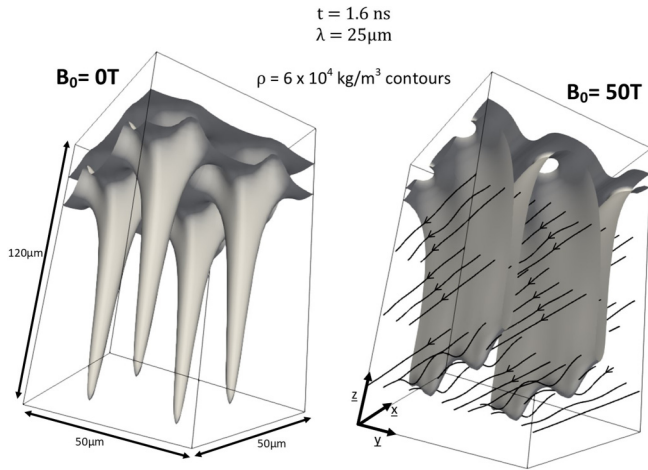
FIG. 1. Density contours $(6 \times 10^4 \text{ kg/m}^3)$ at 1.6 ns for simulations with 25 μm perturbation wavelengths. On the left is the case without an applied field, and on the right is the case using a 50 T magnetic field along $\underline{x}$. The perturbation is almost completely stabilized by magnetic tension in $\underline{x}$ but remains unsuppressed in $\underline{y}$. Two-dimensional simulations ignore the $\underline{y}$ direction.

$\lambda = 50 \, \mu\text{m}$. The height is measured using the 1 keV electron temperature contour. In the $\underline{y}$ direction [Fig. 2(b)] the spike is affected by only classical growth and ablative stabilization. At later times the thermal ablative stabilization becomes more dominant, as the plasma temperature increases. The applied field suppresses the heat flow that drives ablation, resulting in a spike-bubble depth that for the 50 T case is 60% larger than the unmagnetized spike at 2.1 ns. At this time the Hall parameter near the spike tip is approximately 4, which suppressed the heat flow by more than 95% ($\kappa_\perp/\kappa_\parallel < 0.05$).

In the $\underline{x}$ direction [Fig. 2(a)] the spike is also affected by magnetic tension. The applied field acts both to decrease the thermal ablative stabilization and to increase the magnetic tension stabilization. For the 5 T case these contributions roughly cancel, giving a spike height that is similar to the unmagnetized simulation at all times. For 50 T there is significant stabilization even at early times, resulting in anisotropic perturbation growth; the ratio of the height in $\underline{y}$ to the height in $\underline{x}$ is $h_y/h_x > 15$ by 2.1 ns.

Resistive diffusion of the magnetic field is found to play an important role in mitigating the effectiveness of magnetic stabilization. Figure 2(a) includes a plot of the 30 T spike-bubble height when the magnetic diffusivity has been artificially reduced by a factor of 10 in the simulations. The diffusion allows for the perturbations to push through the field lines and increases in importance with time. With resistive diffusion reduced, the peak spike height along the field lines is smaller and occurs approximately 0.15 ns earlier in time, with the perturbation suppressed thereafter. Changes in resistive diffusion are not found to significantly modify the perturbation growth perpendicular to the magnetic field.

To understand how magnetic tension and magnetized ablative stabilization vary for different length-scale perturbations, 3D single-mode simulations have been completed over the range $\lambda = 25\text{--}100 \, \mu\text{m}$. The resultant bubble-spike heights along $\underline{x}$ and $\underline{y}$ are plotted in Fig. 3 at 1.9 ns. Both magnetic
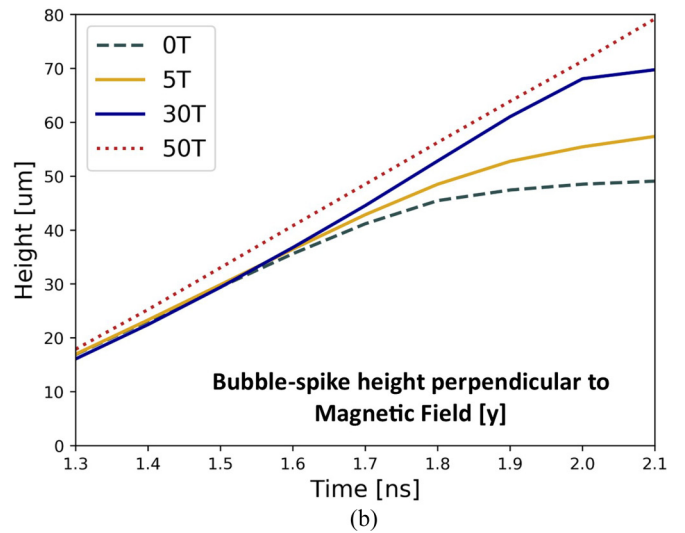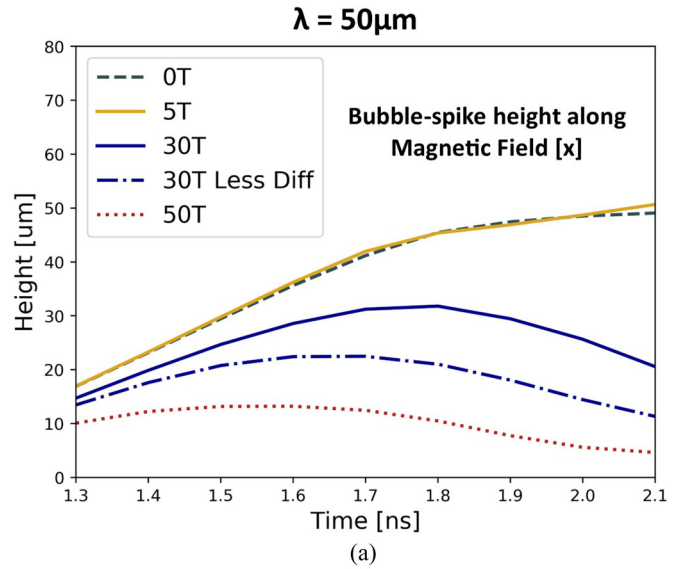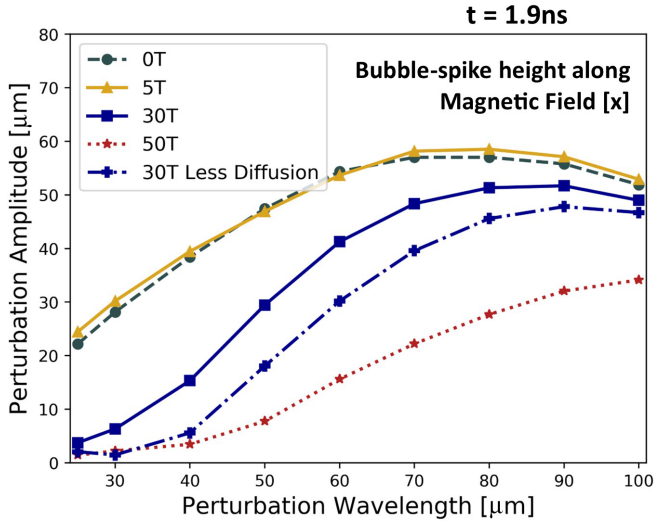

FIG. 2. Bubble-spike height measured by the 1 keV electron temperature contour as a function of time for a range of applied field strengths. The perturbation wavelength here is $\lambda = 50 \, \mu\text{m}$. (a) Bubble-spike height along the direction of the applied field ($\underline{x}$). Magnetic tension stabilizes the perturbation in this orientation. (b) Bubble-spike height perpendicular to the applied field ($\underline{y}$). Magnetization of the electrons results in reduced ablative stabilization at higher field strengths.

tension and ablative stabilization become very important at shorter wavelengths. In $\underline{y}$ the magnetic tension does not affect the perturbation growth; therefore, the applied field increases the bubble-spike height. In $\underline{x}$ the effect of magnetic tension dominates over the reduced ablative stabilization for all wavelengths with 30 and 50 T applied fields.

Also plotted in Fig. 3(a) is the 30 T bubble-spike height in $\underline{x}$ with the resistive diffusion reduced by a factor of 10. A simple scaling has the diffusion timescale behaving as $t_{\text{diff}} \sim \eta/\lambda L_\rho$, where L_ρ is the density length scale. This is consistent with the 3D simulations, with the shortest wavelengths proportionately the most affected by the diffusion. For $\lambda = 40 \, \mu\text{m}$ the spike-bubble height increases by 10 μm due to diffusion, while for

(a)
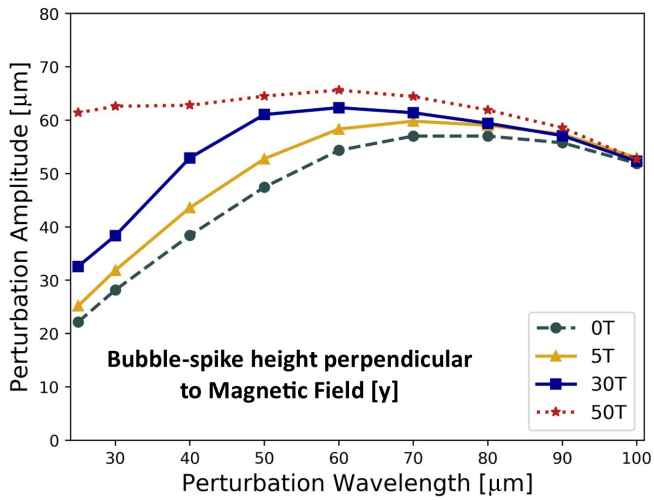
(b)

FIG. 3. Single-mode bubble-spike height measured by the 1 keV electron temperature contour for a range of perturbation wavelengths and applied fields. (a) Bubble-spike height along the direction of the applied field ($\underline{x}$). A 30 T case where the magnetic resistivity has been artificially reduced by a factor of 10 is included to demonstrate the importance of this process in systems with large magnetic tension. (b) Bubble-spike height perpendicular to the applied field ($\underline{y}$). Ablative stabilization has increased importance at short wavelengths.

$\lambda = 100 \,\mu$m the impact of diffusion changes the perturbation amplitude by 2 μm.

So far the discussion of magnetized electron heat flow has been restricted to the suppression of thermal conduction perpendicular to field lines. Here it is also noted that the Righi-Leduc heat flow [the $\kappa_\wedge$ term in Eq. (4)] modifies perturbation growth, particularly for short wavelengths. Figure 4 shows a 2D $\underline{y}$-$\underline{z}$ slice through a simulation with a perturbation wavelength of 25 μm at $t = 2.1$ ns. The applied field is 30 T out of the page. The orientation of Righi-Leduc heat flow, which breaks the left-right symmetry of the spike, is depicted. Qualitatively, electrons that stream along $\underline{z}$ into the spike are
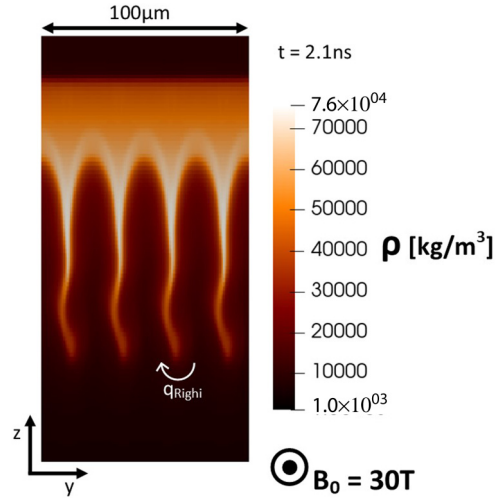

FIG. 4. Two-dimensional slice of mass density of a single-mode perturbation at 2.1 ns with a 30 T magnetic field applied out of the page. The Righi-Leduc heat-flow vector is shown, which acts to break the perturbation symmetry.

deflected left by the magnetic field [26]. Righi-Leduc heat flow results in greater ablation on the left side of the spike than the right, which introduces a higher mode. For the cases simulated, the 30 T applied field gives the greatest effect, with 5 T resulting in too low magnetizations and 50 T then suppressing the Righi-Leduc coefficient.

Biermann battery magnetic fields have been included in all of the simulations results in this paper. The self-generated fields do moderately change the perturbation propagation. However, the process is detailed and will be the subject of a future publication. It suffices to say here that the impact of the Biermann battery is of secondary importance to the applied magnetic field and does not significantly change in significance depending on the applied field strength.

III. MULTIMODE PERTURBATIONS

Multimode simulations use a domain with a 200 μm extent in both $\underline{x}$ and $\underline{y}$. The perturbation is initialized using 500 individual modulations, each with an amplitude randomly chosen between $\pm\epsilon$. The wavelength is chosen randomly in the range of 4–200 μm, and the central location is chosen randomly in $\underline{x}$ and $\underline{y}$. Only one full wavelength of each cosine perturbation is applied, leaving the rest of the domain unperturbed. Both the initialization and evolution use periodic boundary conditions, such that the behavior at the domain edge is not affected by the boundary. A 1/2 μm resolution is used in $\underline{x}$ and $\underline{y}$; 1 μm resolution is used in $\underline{z}$. The simulations were executed for multiple maximum perturbation sizes, $\epsilon = 0.2, 0.5, 1.0, 4.0 \,\mu$m, with the random number generator staying the same between runs in order to keep the same distribution of modes.

Density contours of $\rho = 6 \times 10^{14} \,\text{kg/m}^3$ are compared in Fig. 5 at 1.9 ns for 0 and 50 T with initial perturbation size $\epsilon = 0.5 \,\mu$m. Similar to the single-mode case, the magnetic field suppresses perturbation growth in $\underline{x}$, forming striations with only small amplitude modulations. In $\underline{y}$, however, the
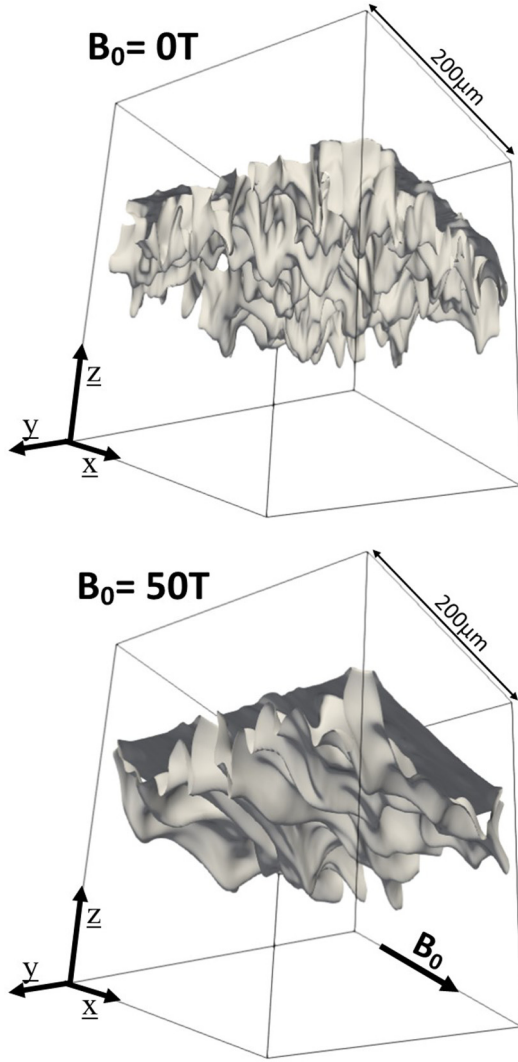
FIG. 5. Density contours (6×10^4 kg/m^3) at 1.9 ns for simulations perturbed with a multitude of modes. Top: no magnetic field applied. Bottom: 50 T magnetic field applied along $\underline{x}$. These simulations use maximum initial perturbation sizes of $\epsilon = 0.5 \, \mu$m.
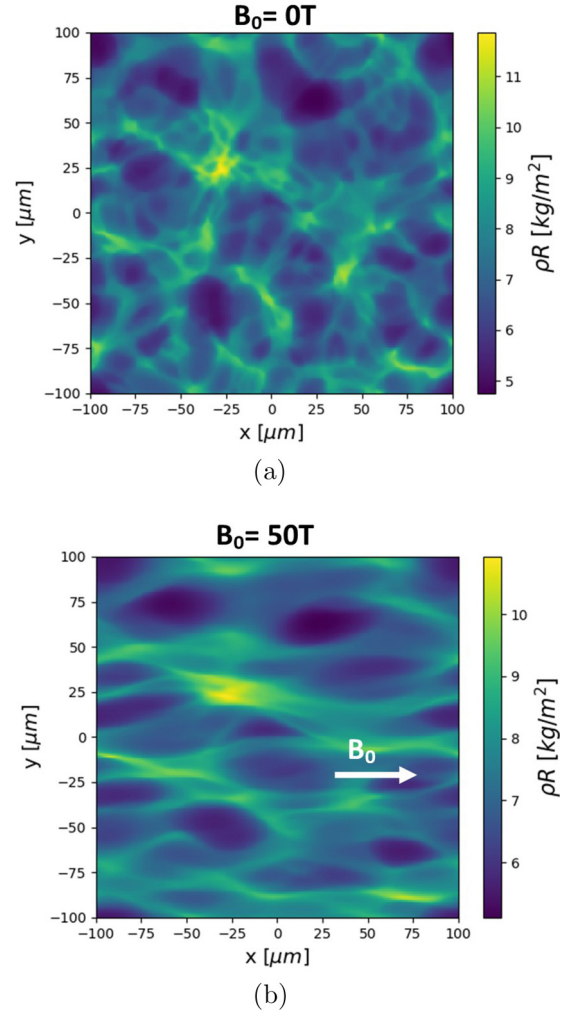

FIG. 6. Mass density of a multimode simulations integrated along $\underline{z}$ to get the areal density with an applied field of (a) 0 T and (b) 50 T. The initial perturbation size is set using $\epsilon = 0.5 \, \mu$m. The data are plotted here at 1.6 ns. The magnetic field (applied from left to right) causes perturbation striations to grow.

bubble-spike amplitudes are similar to those in the unmagnetized case.

To further show the developed striations, the density is integrated along $\underline{z}$ at 1.6 ns, giving areal density as a function of $\underline{x}$ and y. Figure 6 compares this result with and without the 50 T applied field. When no magnetic field is imposed [Fig. 6(a)], the perturbation growth has no preferential orientation. For a 50 T applied field [Fig. 6(b)], the striations clearly form, oriented along the applied field direction.

This behavior can be quantified by taking the Fourier transform of this areal density along $\underline{x}$ and y. It is plotted normalized to the 0 T case in Fig. 7 at 1.6 ns for different initialized perturbation amplitudes. The suppression of perturbations along the magnetic field lines is severe, particularly for modes greater than 5. For the largest applied perturbation size, $\epsilon = 4.0 \, \mu$m, the suppression is much less significant, only approximately 50% lower than in the unmagnetized case.

Perpendicular to the magnetic field ($\underline{y}$) the impact of the magnetic field is also found to be dependent on the initial per-

turbation size. For $\epsilon = 4 \, \mu$m the ablative stabilization reduced by electron magnetization allows for the instability to grow larger, by around 30%–40% at 1.6 ns; this result is consistent with the findings in Sec. II for single-mode perturbations.

As the initial perturbation size is lowered, however, the spike height in the y direction is lowered by magnetization. For $\epsilon = 0.2 \, \mu$m the suppression is up to 50% with a 50 T magnetic field. A strong applied field results in the instability growing in only two dimensions (although not the two dimensions simulated by 2D simulations [2,9]). It has long been known that the Rayleigh-Taylor instability grows slower in two dimensions than in three dimensions [20,21,45]. A factor of around 2–3 has been observed in previous nonlinear simulations comparing dimensionality [45]. Therefore, the suppression of spike-bubble height in $\underline{x}$ can have a moderate and indirect impact on the spike height in y. However, for larger amplitude perturbations (as seen in Fig. 7), the changes in thermal ablative stabilization dominate. At later times, too, the impact of ablative stabilization is more significant (see
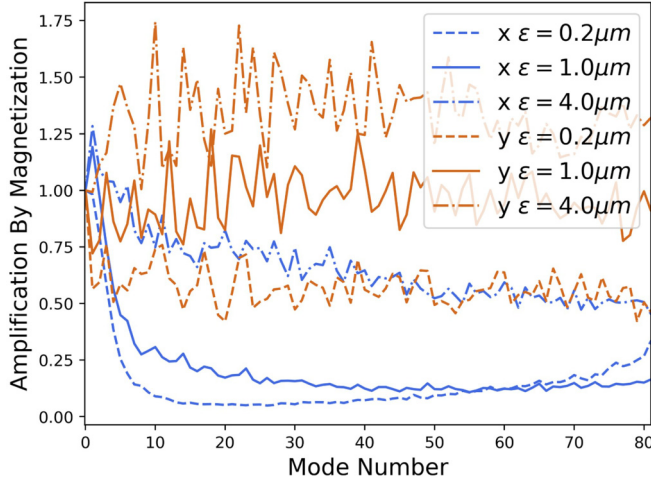
FIG. 7. Amplification of ρR variation due to magnetic field as a function of mode number at 1.6 ns for a 50 T applied field along $\underline{x}$. Perturbations along $\underline{x}$ and $\underline{y}$ are shown separately, with modulations in $\underline{x}$ almost completely suppressed, while perturbations in $\underline{y}$ are only moderately hindered by the magnetic field.

Fig. 2); therefore, the increase in perturbation growth due to suppression of ablation is larger.

IV. CONCLUSIONS

In summary, the magnetized ablative-Rayleigh-Taylor instability was simulated in three dimensions. Previous 2D simulations overpredicted the impact of magnetic tension stabilization by ignoring the most unstable dimension [2,3,8,9]. For spike modes perpendicular to the magnetic field ($\hat{k} \cdot \hat{b} = 0$) growth is, at best, reduced from a 3D growth rate to 2D, which is approximately a factor of 2 smaller. For larger perturbation amplitudes, where the thermal ablative stabilization is more important, the peak bubble-spike height can be increased by magnetization.

Short wavelengths were shown to be the most affected by magnetization. The magnetic tension stabilizes along the field direction but reduces ablative stabilization perpendicularly, resulting in anisotropies in spike-bubble heights $h_y/h_x > 30$ in the most extreme cases simulated.

Resistive diffusion was also found to modify the magnetic tension stabilization. This is particularly true for short wavelengths and long timescale evolution, where the resistivity allows the spike to push through the magnetic field. Righi-Leduc heat flow was also shown to induce higher modes on spikes that have electron magnetizations $\omega_e \tau_e \approx 1$.

These results have significant implications for magnetized spherical and cylindrical implosions on laser and pulsed-power ICF facilities [1,2,13,15]. While magnetic fields are still anticipated to increase fusion performance, the impact of fields on perturbation growth was shown here to be dependent on the perturbation mode number, amplitude, and applied field strength. For spherical implosions dominated by axisymmetric asymmetries (such as low convergence indirect-drive implosions on the National Ignition Facility) 2D simulations including the magnetic tension stabilization may be sufficient; $P2$ and $P4$ low-mode asymmetries as well as the tent scar fall

into this category [46–48]. However, assessing the impact of a magnetic field on surface roughness, beam imprint, or fill-tube asymmetries [46,49] will require 3D calculations. In cases where this is intractable, 2D calculations should be conducted both with and without the Lorentz force included in order to assess the extreme cases.

The impact of an applied magnetic field on the mix induced by a fill tube is of particular interest to the ICF community; as the fill tube is attached to the capsule waist, it will propagate perpendicular to an external magnetic field. The induced short wavelength features that are responsible for the mix of high-Z material into the hot spot are expected to be highly susceptible to stabilization along the magnetic field lines. Perpendicular to the field, however, the impact of the magnetic field is less clear. This work motivates the execution of computationally intensive 3D simulations of a magnetized fill tube in order to shed light on the potential gains of magnetizing ICF targets.

Note that these simulations did not include radiation transport or α heating, both of which increase the ablation of cold fuel into the hot spot. In particular, radiation transport is uninhibited by the magnetic field and will likely lessen the destabilizing effect of the magnetic field for perpendicular modes.

Skepticism of applied magnetic fields suppressing perturbation growth is valid only for cases where the angle between the perturbation mode and magnetic field is constant throughout the instability history. If a multimode surface has a strong magnetic field along $\underline{x}$ at early times, the peak growth will be along $\underline{y}$. If, at late times, the magnetic field then moves to being oriented along $\underline{y}$, the peak bubble-spike height will be suppressed by the field. In MagLIF, for example, a perturbation seeded on the outside of the liner feeds through to the inside surface late in time [4]. As the magnetic field orientation is different on the inside and outside, this constitutes a changing orientation of magnetic field suppression throughout the instability's history. In laser-driven implosions this can occur from twisting of the magnetic field from the cross-gradient-Nernst [38] or Hall term [14].

[1] P. Y. Chang, G. Fiksel, M. Hohenberger, J. P. Knauer, R. Betti, F. J. Marshall, and D. D. Meyerhofer, Fusion Yield Enhancement in Magnetized Laser-Driven Implosions, Phys. Rev. Lett. **107**, 035006 (2011).

[2] L. J. Perkins, D. D.-M Ho, B. G. Logan, G. B. Zimmerman, M. A. Rhodes, D. J. Strozzi, D. T. Blackfield, and S. A. Hawkins, The potential of imposed magnetic fields for enhancing ignition probability and fusion energy yield in indirect-drive inertial confinement fusion, Phys. Plasmas **24**, 062708 (2017).

[3] L. J. Perkins, B. G. Logan, G. B. Zimmerman, and C. J. Werner, Two-dimensional simulations of thermonuclear burn in ignition-scale inertial confinement fusion targets under compressed axial magnetic fields, Phys. Plasmas **20**, 072708 (2013).

[4] M. R. Gomez *et al.*, Performance Scaling in Magnetized Liner Inertial Fusion Experiments, Phys. Rev. Lett. **125**, 155002 (2020).

[5] S. A. Slutz *et al.*, Enhancing performance of magnetized liner inertial fusion at the Z facility, Phys. Plasmas **25**, 112706 (2018).

[6] D. H. Barnak, J. R. Davies, R. Betti, M. J. Bonino, E. M. Campbell, V. Yu. Glebov, D. R. Harding, J. P. Knauer, S. P. Regan, A. B. Sefkow, A. J. Harvey-Thompson, K. J. Peterson, D. B. Sinars, S. A. Slutz, M. R. Weis, and P.-Y. Chang, Laser-driven magnetized liner inertial fusion on OMEGA, Phys. Plasmas **24**, 056310 (2017).

[7] W.-M. Wang, P. Gibbon, Z.-M. Sheng, and Y.-T. Li, Magnetically Assisted Fast Ignition, Phys. Rev. Lett. **114**, 015001 (2015).

[8] J. Narkis, F. Conti, A. L. Velikovich, and F. N. Beg, Mitigation of magneto-Rayleigh-Taylor instability growth in a triple-nozzle, neutron-producing gas-puff Z pinch, Phys. Rev. E **104**, L023201 (2021).

[9] B. Srinivasan and X.-Z. Tang, The mitigating effect of magnetic fields on Rayleigh-Taylor unstable inertial confinement fusion plasmas, Phys. Plasmas **20**, 056307 (2013).

[10] S. Chandrasekhar and J. Gillis, Hydrodynamic and hydromagnetic stability, Phys. Today **15**(3), 58 (1962).

[11] C. A. Walsh, K. Mcglinchey, J. K. Tong, B. D. Appelbe, A. Crilly, M. Zhang, and J. P. Chittenden, Perturbation modifications by pre-magnetisation in inertial confinement fusion implosions, Phys. Plasmas **26**, 022701 (2019).

[12] J. R. Davies, R. Betti, P.-Y. Chang, and G. Fiksel, The importance of electrothermal terms in Ohm's law for magnetized spherical implosions, Phys. Plasmas **22**, 112703 (2015).

[13] J. R. Davies, D. H. Barnak, R. Betti, E. M. Campbell, P.-Y. Chang, A. B. Sefkow, K. J. Peterson, D. B. Sinars, and M. R. Weis, Laser-driven magnetized liner inertial fusion, Phys. Plasmas **24**, 062701 (2017).

[14] C.Walsh, R. Florido, M. Bailly-Grandvaux, F. Suzuki-Vidal, J. P. Chittenden, A. Crilly, M. A. Gigosos, R. Mancini, G. Perez-Callejo, C. Vlachos, C. McGuffey, F. N. Beg, and J. J. Santos, Exploring extreme magnetization phenomena in directly-driven imploding cylindrical targets, Plasma Phys. Controlled Fusion (2021), doi: 10.1088/1361-6587/ac3f25.

[15] S. A. Slutz, M. C. Herrmann, R. A. Vesey, A. B. Sefkow, D. B. Sinars, D. C. Rovang, K. J. Peterson, and M. E. Cuneo, Pulsed-power-driven cylindrical liner implosions of laser preheated fuel magnetized with an axial field, Phys. Plasmas **17**, 056303 (2010).

[16] S. A. Slutz, W. A. Stygar, M. R. Gomez, K. J. Peterson, A. B. Sefkow, D. B. Sinars, R. A. Vesey, E. M. Campbell, and R. Betti, Scaling magnetized liner inertial fusion on Z and future pulsed-power accelerators, Phys. Plasmas **23**, 022702 (2016).

[17] S. A. Slutz and R. A. Vesey, High-Gain Magnetized Inertial Fusion, Phys. Rev. Lett. **108**, 025003 (2012).

[18] T. Johzaki, H. Nagatomo, A. Sunahara, Y. Sentoku, H. Sakagami, M. Hata, T. Taguchi, K. Mima, Y. Kai, D. Ajimi, T. Isoda, T. Endo, A. Yogo, Y. Arikawa, S. Fujioka, H. Shiraga, and H. Azechi, Integrated simulation of magnetic-field-assist fast ignition laser fusion, Plasma Phys. Controlled Fusion **59**, 014045 (2017).

[19] J. M. Stone and T. Gardiner, Nonlinear evolution of the magnetohydrodynamic Rayleigh-Taylor instability, Phys. Fluids **19**, 094104 (2007).

[20] Y. Zhou, Rayleigh-Taylor and Richtmyer-Meshkov instability induced flow, turbulence, and mixing. I, Phys. Rep. **720–722**, 1 (2017).

[21] Y. Zhou, T. T. Clark, D. S. Clark, S. G. Glendinning, M. A. Skinner, C. M. Huntington, O. A. Hurricane, A. M. Dimits, and B. A. Remington, Turbulent mixing and transition criteria of flows induced by hydrodynamic instabilities, Phys. Plasmas **26**, 080901 (2019).

[22] J. Sanz, Self-consistent Analytical Model of the Rayleigh-Taylor Instability in Inertial Confinement Fusion, Phys. Rev. Lett. **73**, 2700 (1994).

[23] J. K. Tong, K. McGlinchey, B. D. Appelbe, C. A. Walsh, A. J. Crilly, and J. P. Chittenden, Burn regimes in the hydrodynamic scaling of perturbed inertial confinement fusion hotspots, Nucl. Fusion **59**, 086015 (2019).

[24] R. Betti, M. Umansky, V. Lobatchev, V. N. Goncharov, and R. L. McCrory, Hot-spot dynamics and deceleration-phase Rayleigh-Taylor instability of imploding inertial confinement fusion capsules, Phys. Plasmas **8**, 5257 (2001).

[25] F. Modica, T. Plewa, and A. Zhiglo, The Braginskii model of the Rayleigh-Taylor instability. I. Effects of self-generated magnetic fields and thermal conduction in two dimensions, High Energy Density Phys. **9**, 767 (2013).

[26] S. I. Braginskii, Transport processes in a plasma, Rev. Plasma Phys. **1**, 205 (1965).

[27] J. D. Sadler, C. A. Walsh, and H. Li, Symmetric Set of Transport Coefficients for Collisional Magnetized Plasma, Phys. Rev. Lett. **126**, 075001 (2021).

[28] E. C. Hansen, J. R. Davies, D. H. Barnak, R. Betti, E. M. Campbell, V. Yu. Glebov, J. P. Knauer, L. S. Leal, J. L. Peebles, A. B. Sefkow, and K. M. Woo, Neutron yield enhancement and suppression by magnetization in laser-driven cylindrical implosions, Phys. Plasmas **27**, 062703 (2020).

[29] F. Conti, N. Aybar, J. Narkis, J. C. Valenzuela, H. U. Rahman, E. Ruskov, E. Dutra, S. Haque, A. Covington, and F. N. Beg, Study of stability in a liner-on-target gas puff Z-pinch as a function of pre-embedded axial magnetic field, Phys. Plasmas **27**, 012702 (2020).

[30] E. S. Lavine, S. V. Rocco, J. T. Banasek, W. M. Potter, J. B. Greenly, H. Wilhelm, N. Qi, D. A. Hammer, and B. R. Kusse, Implosion dynamics of triple-nozzle gas-puff z pinches on CO-BRA, Phys. Plasmas **28**, 022703 (2021).

[31] C. A. Walsh, A. J. Crilly, and J. P. Chittenden, Magnetized directly-driven ICF capsules: Increased instability growth from non-uniform laser drive, Nucl. Fusion **60**, 106006 (2020).

[32] J. P. Chittenden, S. V. Lebedev, C. A. Jennings, S. N. Bland, and A. Ciardi, X-ray generation mechanisms in three-dimensional simulations of wire array Z-pinches, Plasma Phys. Controlled Fusion **46**, B457 (2004).

[33] A. Ciardi, S. V. Lebedev, A. Frank, E. G. Blackman, J. P. Chittenden, C. J. Jennings, D. J. Ampleford, S. N. Bland, S. C. Bott, J. Rapley, G. N. Hall, F. A. Suzuki-Vidal, A. Marocchino, T. Lery, and C. Stehle, The evolution of magnetic tower jets in the laboratory, Phys. Plasmas **14**, 056501 (2007).

[34] C. A. Walsh, J. P. Chittenden, K. McGlinchey, N. P. L. Niasse, and B. D. Appelbe, Self-Generated Magnetic Fields in the Stagnation Phase of Indirect-Drive Implosions on the National Ignition Facility, Phys. Rev. Lett. **118**, 155001 (2017).

[35] C. A. Walsh, J. P. Chittenden, D. W. Hill, and C. Ridgers, Extended-magnetohydrodynamics in under-dense plasmas, Phys. Plasmas **27**, 022103 (2020).

[36] J. D. Sadler, H. Li, and K. A. Flippo, Magnetic field generation from composition gradients in inertial confinement fusion fuel, Philos. Trans. R. Soc. A **378**, 20200045 (2020).

[37] C. A. Walsh and D. S. Clark, Biermann battery magnetic fields in ICF capsules: Total magnetic flux generation, Phys. Plasmas **28**, 092705 (2021).

[38] C. A. Walsh, J. D. Sadler, and J. R. Davies, Updated magnetized transport coefficients: Impact on laser-plasmas with self-generated or applied magnetic fields, Nucl. Fusion **61**, 116025 (2021).

[39] P. T. Campbell, C. A. Walsh, B. K. Russell, J. P. Chittenden, A. Crilly, G. Fiksel, L. Gao, I. V. Igumenshchev, P. M. Nilson, A. G. R. Thomas, K. Krushelnick, and L. Willingale, Measuring magnetic flux suppression in high-power laser-plasma interactions, Physics of Plasmas **29**, 012701 (2022).

[40] P. T. Campbell, C. A. Walsh, B. K. Russell, J. P. Chittenden, A. Crilly, G. Fiksel, P. M. Nilson, A. G. R. Thomas, K. Krushelnick, and L. Willingale, Magnetic Signatures of Radiation-Driven Double Ablation Fronts, Phys. Rev. Lett. **125**, 145001 (2020).

[41] E. M. Epperlein and M. G. Haines, Plasma transport coefficients in a magnetic field by direct numerical solution of the Fokker-Planck equation, Phys. Fluids **29**, 1029 (1986).

[42] J. P. Knauer, O. V. Gotchev, P. Y. Chang, D. D. Meyerhofer, O. Polomarov, R. Betti, J. A. Frenje, C. K. Li, M. J.-E. Manuel, R. D. Petrasso, J. R. Rygg, and F. H. Séguin, Compressing magnetic fields with high-energy lasers, Phys. Plasmas **17**, 056318 (2010).

[43] P. Sharma and G. W. Hammett, Preserving monotonicity in anisotropic diffusion, J. Comput. Phys. **227**, 123 (2007).

[44] C. A. Walsh, Extended Magneto-hydrodynamic Effects in Indirect-Drive Inertial Confinement Fusion Experiments.

[45] N. N. Anuchina, V. I. Volkov, V. A. Gordeychuk, N. S. Es'kov, O. S. Ilyutina, and O. M. Kozyrev, Numerical simulations of Rayleigh-Taylor and Richtmyer-Meshkov instability using MAH-3 code, J. Comput. Appl. Math. **168**, 11 (2004).

[46] D. S. Clark, C. R. Weber, J. L. Milovich, J. D. Salmonson, A. L. Kritcher, S. W. Haan, B. A. Hammel, D. E. Hinkel, O. A. Hurricane, O. S. Jones, M. M. Marinak, P. K. Patel, H. F. Robey, S. M. Sepke, and M. J. Edwards, Three-dimensional simulations of low foot and high foot implosion experiments on the National Ignition Facility, Phys. Plasmas **23**, 056302 (2016).

[47] M. Gatu Johnson *et al.*, Impact of imposed mode 2 laser drive asymmetry on inertial confinement fusion implosions, Phys. Plasmas **26**, 012706 (2019).

[48] M. Gatu Johnson, B. D. Appelbe, J. P. Chittenden, J. Delettrez, C. Forrest, J. A. Frenje, V. Yu. Glebov, W. Grimble, B. M. Haines, I. Igumenshchev, R. Janezic, J. P. Knauer, B. Lahmann, F. J. Marshall, T. Michel, F. H. Séguin, C. Stoeckl, C. Walsh, A. B. Zylstra, and R. D. Petrasso, Impact of asymmetries on fuel performance in inertial confinement fusion, Phys. Rev. E **98**, 051201 (2018).

[49] K. McGlinchey, B. Appelbe, A. Crilly, J. Tong, C. Walsh, and J. Chittenden, Diagnostic Signatures of Performance Degrading Perturbations in Inertial Confinement Fusion Implosions, Physics of Plasmas **25**, 122705 (2018).